

# The Partition of Unity Method for High-Order Finite Volume Schemes Using Radial Basis Functions Reconstruction

Serena Morigi<sup>1</sup> and Fiorella Sgallari<sup>2,\*</sup>

<sup>1</sup> *Department of Mathematics, University of Bologna, Pzsa Porta San Donato, 5, Bologna, Italy.*

<sup>2</sup> *CIRAM, University of Bologna, Via Saragozza, 8, Bologna, Italy.*

Received 17 July 2008; Accepted (in revised version) 20 November 2008

---

**Abstract.** This paper introduces the use of partition of unity method for the development of a high order finite volume discretization scheme on unstructured grids for solving diffusion models based on partial differential equations. The unknown function and its gradient can be accurately reconstructed using high order optimal recovery based on radial basis functions. The methodology proposed is applied to the noise removal problem in functional surfaces and images. Numerical results demonstrate the effectiveness of the new numerical approach and provide experimental order of convergence.

**AMS subject classifications:** 65N99, 68U10, 65F22

**Key words:** Finite volume discretization, radial basis functions, optimal recovery, regularization, image and surface denoising.

---

## 1. Introduction

Evolutionary nonlinear partial differential equations (PDEs) are nowadays a well assessed tool in image, surface processing and computer vision. The main image and surface processing applications involving PDE models are nonlinear filtering, edge/feature detection, image deblurring and enhancement, restoration, inpainting, segmentation, shape extraction and analysis, motion analysis, see, e.g., [7, 17, 22]. The time discretization of the PDE models is usually obtained by explicit or implicit methods while the space discretization is provided by finite element (FEM), finite difference (FD) or finite volumes (FV) schemes covering the domain by suitable grids. In image processing structured grids are simple to handle, while in surface processing block structured or unstructured grids are of common usage. FEM and FV methods have been used successfully to solve problems of image multi-scale analysis. In particular, since FV schemes are directly based on the integral form of the conservation law and because the numerical flux is based on the physics of

---

\*Corresponding author. *Email addresses:* [morigi@dm.unibo.it](mailto:morigi@dm.unibo.it) (S. Morigi), [sgallari@dm.unibo.it](mailto:sgallari@dm.unibo.it) (F. Sgallari)

nonlinear wave propagation, the FV schemes are thus able to cope with discontinuities in the solution, and thus are particularly suitable to deal with image or surfaces domains [8].

The goal of our work is to construct a new numerical method, that we name "partition of unity high order finite volume" (PUHOFV) method, which solves PDEs with, at least theoretically, arbitrary high order of accuracy in space on unstructured meshes complex domains. In particular, we investigate certain PDE diffusion models in the context of image and surface denoising. The main ingredient of the proposed PUHOFV scheme is a new reconstruction strategy based on partition of unity and RBF optimal recovery, which makes use of simple regularization techniques allowing for a robust computation on strongly unstructured grids.

The partition of unity framework is a powerful technique to approximate a global function blending together the local approximations; it is able to model discontinuities and singularities through local enrichment. Initially introduced as a general FEM method in computational mechanics, see, e.g., [1, 14], the partition of unity approach has become popular also in the computer graphics community within shape reconstruction setting, [27]. In this work, the partition of unity method is used to provide an easy to use and accurate approximation framework for finite volume schemes on unstructured grids.

The finite volume method is based on the discretization of the solution domain into a set of non-overlapping finite volumes and thereafter, the integral representation of the underlying conservation laws are approximated over these volumes using some appropriate numerical strategy [26]. In the cell-centered approach the computed quantities are stored on each cell and the centroid values of the dependent variable play an important role in the interpolation methods required to reconstruct fluxes. However, a high accuracy reconstruction should be combined with an accurate integral approximation method [25].

Traditionally, the midpoint rule has been the favored method to approximate the line integrals involving these fluxes. However, it achieves second order accuracy only when the flux evaluations are sufficiently accurate. We will consider Gaussian quadrature methods for integration in order to obtain an arbitrary desired precision.

The basic FV schemes offer a piecewise constant solution representation in space; they are very robust but provide only a first order accuracy, thus requiring to refine the grid tremendously to obtain the desired accuracy, with a consequent overhead in time and memory requirements. This leads naturally into the theory of optimal recovery. Since Barth and Frederickson's pioneering work [2], a number of researchers have studied high order FV methods using unstructured meshes. The reason for developing very high order schemes is that they permit a good resolution of physical phenomena even on very coarse grids and that they exhibit only very little numerical dissipation, which is important when performing simulations in large domains for long times. Furthermore, grid refinement becomes much more efficient using high order schemes since numerical errors decrease faster compared to the case when the same grid refinement is applied using a low order scheme.

The key aspect of a high order accurate FV solver is a high order reconstruction by means of piecewise smooth functions from the cell average values. To this aim, a variety of techniques have been explored to reconstruct the fluxes to at least second order accuracy

using some set of suitably chosen local nodal values of the dependent variable. To avoid oscillations introduced by the reconstruction at discontinuities, slope limiters are used to ensure local maximum principles and to guarantee that the total variation of the numerical solution rests at least bounded [10]. This can be obtained by high order polynomial reconstruction using Essentially Non-Oscillatory (ENO) or Weighted Essentially Non-Oscillatory (WENO) techniques [33]. On structured grids a very high order of accuracy can be obtained but on unstructured grids the procedure becomes very complicated.

We investigate the method of radial basis functions (RBFs) reconstruction which leads to high-order gradient and flux approximations. Moreover, the optimal recovery with RBF that we propose employs a particular stencil which avoids the ENO-construction and oscillations.

Radial Basis Functions are a well assessed tool in the scattered data approximation field [6, 13] since they represent a powerful alternative to polynomial reconstruction. For many years, RBFs have also been used to solve PDEs, through the use of collocation methods [11, 12]. However, the RBF-based collocation approach does not share many of the desirable properties of the finite volume method, such as local conservation and the ability to work with small size matrices. Moreover, collocation solution of PDEs can be severely affected by the well known ill-conditioning in the RBF coefficient computations which depends on the location of the point values [30, 31].

The use of RBF local interpolation instead of a global approach, leads to the solution of small size linear systems. However, for severe irregular unstructured grids, the ill-conditioning problems could affect the accuracy of the solution. To this aim, regularized approximations can be obtained by using a truncated singular value decomposition, or more sophisticated regularization procedures [5]. In this work we provide an alternative regularization approach based on least square approximation and splitting interpolation. In the numerical section we will demonstrate how this does not affect the experimental order of convergence obtained by optimal radial recovery.

The remaining of this paper is organized as follows. In Section 2 the governing equations are briefly reviewed, while some basic ingredients of partition of unity are introduced in Section 3. In Section 4, the space discretization based on a finite volume scheme is discussed. The radial recovery strategy is introduced in Section 5 in order to derive a high order finite volume scheme. The proposed regularization procedures to achieve accurate RBF coefficients in case of ill-conditioning are introduced in Section 6. The experimental order of convergence of the PUHOFV method is demonstrated in Section 7, together with the application to a two coupled non-linear second order PDE-model for curvature preserving surface denoising. Section 8 contains concluding remarks.

## 2. Statement of the problem and assumptions

We consider the following nonlinear partial differential equation

$$\frac{\partial u}{\partial t} - \nabla \cdot (g(|\nabla u|) \nabla u - \mathbf{a}) = f(u), \quad (2.1)$$

where  $u(t, x)$  is an unknown function defined in  $[0, t_{MAX}] \times \Omega$ ,  $\mathbf{a}$  represents a generic vector and  $f$  is a given source term.

The equations are accompanied by zero Neumann boundary conditions

$$\frac{\partial u}{\partial \mathbf{n}} = 0 \quad \text{on } [0, t_{MAX}] \times \partial \Omega, \quad (2.2)$$

and initial condition

$$u(0, x) = u_0(x) \quad \text{in } \Omega, \quad (2.3)$$

where  $\mathbf{n}$  is the unit normal to the boundary of the domain  $\Omega$ .

In general,  $g(\cdot)$  can be a nonlinear function of  $u$  or  $\nabla u$ . In the computer vision community, Eq. (2.1) represents the well-known Perona Malik equation [28], called also *anisotropic diffusion*, when  $g(\cdot)$  is of the form

$$g(|\nabla u|) = \frac{1}{1 + K|\nabla u|^2} \quad (2.4)$$

with some constant  $K > 0$ . The diffusion term  $g(\cdot)$  selectively diffuses the gray-values in an image in regions where the signal is of a constant mean in contrast to those regions where the signal changes its tendency (edge).

Another well-known choice for  $g(\cdot)$  is represented by

$$g(|\nabla u|) = \frac{1}{|\nabla u|}, \quad (2.5)$$

which gives rise to the Total Variation (TV) model. The TV image restoration model was first introduced by Rudin, Osher, and Fatemi (ROF) in their pioneering work [34] on edge preserving image denoising. It is one of the earliest and best known examples of PDE-based edge preserving denoising designed with the explicit goal of preserving sharp discontinuities (edges) in images while removing noise and other unwanted fine scale details. The revolutionary aspect of this model is its regularization term that allows for discontinuities but at the same time disfavors oscillations.

In this work, we consider the discretization of (2.1) with the choice (2.5) for the function  $g(\cdot)$ , by the PUHOFV scheme in Section 4. Furthermore, in Section 7, we investigate the application of both the TV model and of a generalization of the two-step model proposed in [20] and [21], to the denoise of images and surfaces.

Our generalization of the two-step model [20] has been introduced in the conference proceeding [24] and consists of two coupled non-linear second order PDEs. The first equation smoothes the normal field of the corrupted surface, while the second equation reconstructs a noise-reduced surface from the smoothed normal field. This model has been proposed for noise removal in digital images where the purpose is to preserve the edges. In the functional surface case the structures that characterize the data are the creases, that is areas of high curvature. The original model will be changed according to this purpose.

### 3. Partition of Unity Method for finite volume reconstruction

A Partition of Unity Method (PUM) is a paradigm in which a domain  $\Omega$  is subdivided into  $N$  overlapping patches, or subdomains  $\Omega_i$ , each of which is associated with a local approximation

$$u_i := \sum_k u_i^k \phi_i^k \quad (3.1)$$

defined by basis functions  $\{\phi_i^k\}$  on a local support  $\Omega_i := \text{supp}\{\phi_i^k\}$ . A global approximation  $u_{PU}$  is simply defined as a weighted sum of the local approximations  $u_i$ , as follows:

$$u_{PU}(x) := \sum_{i=1}^N \omega_i(x) u_i = \sum_{i \in N_x} \omega_i(x) u_i, \quad (3.2)$$

where  $\text{card}(N_x) \ll N$ , and the weight functions  $\omega_i(x)$  form a PU, that is

$$\sum_{i=1}^N \omega_i(x) = 1 \quad \text{in } \Omega. \quad (3.3)$$

Given a set of nonnegative compactly supported functions  $\{W_i(x)\}$  such that  $\Omega \subset \bigcup_i \text{supp}\{W_i\}$ , the *partition of unity functions*  $\omega_i(x)$  can be generated by

$$\omega_i(x) = \frac{W_i(x)}{\sum_{i=1}^N W_i(x)}. \quad (3.4)$$

For the interpolation process, the *inverse-distance singular weights* functions are mainly used (see [29])

$$W_i(x) = \left[ \frac{(\rho_i - |x - c_i|)_+}{\rho_i |x - c_i|} \right]^2, \quad \text{where } (a)_+ = \begin{cases} a & \text{if } a > 0, \\ 0 & \text{otherwise,} \end{cases} \quad (3.5)$$

centered at  $c_i$  and having a spherical support of radius  $\rho_i$ . Besides these weight functions, thin-plate splines, B-splines, and Gaussians can be considered in PU methods.

The PU functions  $\omega_i(x)$  are used to blend together the local approximations  $u_i$  in such a way that the global approximation  $u_{PU}$  benefits from the local approximation orders, that can be independent of each local  $u_i$ , and satisfies global regularity conditions.

A key issue concerning PU methods in the context of finite volume schemes on unstructured grids is the definition of neighborhood nodes for each evaluation point. Considering a cell-centered approach with triangle finite volumes, the nodes are the centroids of the volumes. Thus for each evaluation point  $x$ , the global solution given by (3.2) requires the evaluation at  $x$  of a certain set  $N_x$  of PU functions.  $N_x$  in (3.2) represents the set of indexes of all the neighbors triangles whose influence region  $\Omega_i$  contains  $x$ . In the following we will refer to this region of influence as the *stencil*.

The gradient of  $u_{pU}$  can be evaluated as

$$\nabla u_{pU}(x) := \sum_{i=1}^N \nabla \omega_i(x) u_i = \sum_{i \in N_x} \nabla \omega_i(x) u_i. \quad (3.6)$$

Instead of this constant reconstruction we introduce in Section 5 a radial basis function interpolation  $u_i$  which is infinitely differentiable, thus allowing us to obtain accurate gradient reconstructions. Higher order derivatives could be computed in a similar way.

Note that both the reconstructed values of  $u(x)$  and its derivatives at a certain location are obtained using the information from neighboring nodes, and the weights are function of distances between nodes, with no reference to any grid-based data structure. Thus this approach could be extended to a meshless framework. However, in this work, we used a mesh-based approach only for the construction of the local approximation  $u_i$  in (3.1), which requires only a local mesh definition. For practical purposes, the entire mesh is initially pre-computed.

The PU approach for solving differential equations, falls in the category of "meshless" methods; a mesh in a classical sense does not have to be created and thus the complicating meshing process is avoided. Truly meshfree Galerkin methods, which are based only on a set of irregularly spaced points, have to deal with the construction of a cover from a given set of points that involves neighboring searching and sorting problems [14, 15]. To cope with these problems, complex data structures have to be constructed and handled. Moreover, in meshfree Galerkin methods the assembly of the stiffness matrix and the right-hand side vector is one major issue of concern with PUM, because this process requires the more complicated integration of the product functions  $\omega_i(x)\phi_i(x)$  [19]. Hence the meshfree Galerkin methods are so far more expensive than the mesh-based ones. Only in special cases can be worthwhile to tackle these problems; for example, when a refinement/coarsening of the data set is required, or for particle methods in a Lagrangian approach, or for high dimension domains, (e.g.,  $\mathbb{R}^d, d \geq 3$ ).

In this paper we propose to utilize the partition of unity approach in a mesh-based FV method to benefit of the high order local approximants to reconstruct a high order FV-based global solution  $u_{pU}$  from the cell average values, in a natural and inexpensive way.

#### 4. Finite volume discretization

According to the classical Finite Volume (FV) discretization, the computational domain  $\Omega \subset \mathbb{R}^2$ , that we assume for simplicity bounded by a piecewise polygonal curve, is first tessellated into a collection  $\mathcal{T}$  of non-overlapping triangles  $T_i, i = 1, \dots, \mathcal{N}$ , defined as *control volumes*, so that

$$\Omega = \bigcup_{i=1}^{\mathcal{N}} T_i \quad (4.1)$$

which form an unstructured mesh characterized by a mesh width  $h$ . The triangles  $T_i$  represent the primal mesh. In the cell-centered finite volume schemes the triangle themselves

serve as control volumes with unknown solutions stored on each triangle. Other finite volume schemes which consider the dual mesh, have been successfully applied to the image processing field [17].

Fundamental to finite volume schemes is the introduction of the so-called *cell average* operator for each  $T_i \in \mathcal{T}$ , defined as follows:

$$L_i u = \bar{u}_i(t) := \frac{1}{|T_i|} \int_{T_i} u(t, \mathbf{x}) d\mathbf{x}, \quad (4.2)$$

where  $|T_i|$  denotes the area of the  $i$ th triangle. In order to establish mass conservation, corresponding cell average values of the numerical solution are maintained during the evolution. The total mass contained in the cell  $T_i$  at time  $t$ , is then given by

$$m_{T_i}(t) = |T_i| \cdot \bar{u}_i(t) \quad \forall T_i \in \mathcal{T}. \quad (4.3)$$

Therefore the total mass over the entire domain  $\Omega$  at time  $t$  is  $\sum_{T_i \in \mathcal{T}} m_{T_i}(t)$ .

The finite volume spatial discretization of the model problem (2.1) with (2.5) proceeds by integrating on the generic control volume  $T_i \in \mathcal{T}$ , and applying the Gauss-Green theorem, we get

$$\frac{d\bar{u}(t)}{dt} - \frac{1}{|T_i|} \sum_{j \in N(i)} \int_{e_{ij}} \left( \frac{\nabla u}{|\nabla u|} - \mathbf{a} \right) \cdot \mathbf{n} ds = \frac{1}{|T_i|} \int_{T_i} f dx, \quad (4.4)$$

where  $e_{ij} = \partial T_i \cap \partial T_j$  is the common edge between triangles  $T_i$  and  $T_j$ ,  $\mathbf{n} = (nx, ny)^T$  is the outer unit normal vector on the edge  $e_{ij}$ , and  $N(i) = \{j \in \mathbb{N} | e_{ij} \text{ is edge of } T_i\}$ . In order to numerically compute the line integral in (4.4) on the edge  $e_{ij}$  we use Gaussian quadrature of the form

$$\int_e G(\phi(s)) ds = \sum_{k=1}^{ng} w_k G(\phi(s_k)) + \mathcal{O}(h^{2ng}), \quad (4.5)$$

where  $ng$  denotes the number of integration nodes,  $w_k$  are certain quadrature weights, and  $h$  is in this case the length of the control volume edge. In particular, on the edge  $e_{ij}$  defined by the vertices  $\mathbf{x}_i, \mathbf{x}_j$ , a three-point Gaussian quadrature in the interval  $[-1, 1]$  is applied and the integral nodes are then given by the parametrization

$$p_{ij}(s) = \frac{1}{2}(\mathbf{x}_i + \mathbf{x}_j) + \frac{s}{2}(\mathbf{x}_j - \mathbf{x}_i). \quad (4.6)$$

The integral term on the left-hand side of Eq. (4.4) becomes:

$$\frac{1}{|T_i|} \sum_{j \in N(i)} \int_{-1}^1 \left( \frac{u_x(p_{ij}(s))}{|\nabla u|} nx + \frac{u_y(p_{ij}(s))}{|\nabla u|} ny - \mathbf{a} \cdot \mathbf{n} \right) ds.$$

Applying the quadrature rule (4.5) we get

$$\frac{1}{|T_i|} \sum_{j \in N(i)} \frac{|e_{ij}|}{2} \left\{ \sum_{k=1}^{ng} w_k \frac{u_x(p_{ij}(s_k), t)nx + u_y(p_{ij}(s_k), t)ny}{\sqrt{u_x(p_{ij}(s_k), t)^2 + u_y(p_{ij}(s_k), t)^2}} + \mathcal{O}(h^{2ng}) \right\} + |e_{ij}|(\mathbf{a} \cdot \mathbf{n}).$$

The integral term on the right-hand side of equation (4.4) can be accurately computed in a similar way by a two-dimensional Gaussian quadrature formula ensuring that the errors in computing (4.4) are due to inaccuracies in the integral term on the left-hand side. In this work we used a seven points Gaussian quadrature rule.

According to the classical conservation theory literature [32], a numerical approximation of the flux function in (4.4) can be obtained by basic finite volume method replacing the unknown values  $u(p(s_k), t)$  simply by the cell averages, that is  $F(\bar{u}, \bar{u}; \mathbf{n})$ , thus obtaining the following semi-discrete finite volume basic scheme.

**Definition 4.1. Basic FV.** *The semi-discrete finite volume approximation of (4.4) utilizing continuous in time solution representation,  $t \in [0, +\infty)$ , and piecewise constant solution representation in space  $u_h$ , such that*

$$\bar{u}_j(t) = \frac{1}{|T_j|} \int_{T_j} u_h(x, t) dx,$$

with initial data  $\bar{u}_j(0) = \frac{1}{|T_j|} \int_{T_j} u_0(x) dx$ , and suitable boundary conditions, is given by the following system of ordinary differential equations

$$\frac{d\bar{u}_i}{dt} - \frac{1}{|T_i|} \sum_{j \in N(i)} |e_{ij}| \sum_{k=1}^{ng} w_k F(\bar{u}_i, \bar{u}_j; \mathbf{n}_{ij}) = \frac{1}{|T_i|} \sum_{j \in N(i)} w_k f_k, \quad \forall T_i \in \mathcal{T}. \quad (4.7)$$

The finite volume scheme provide an approximation of the cell average of  $u$  on  $T_i$  denoted by  $u_i$ . The piecewise constant solution  $u_h$  collects all the approximate cell averages, i.e.,  $u_h|_i = u_i$ . If the weak solution  $u$  and the numerical flux function  $F$  are continuously differentiable, then the basic finite volume method is of first order in space [32].

More accurate methods, that is high order schemes, can be devised by using sufficiently accurate flux evaluations, through a suitable reconstruction procedure.

#### 4.1. Reconstruction

An accurate final solution representation is usually obtained by substituting the piecewise constant representation of the basic first-order scheme with a piecewise smooth reconstruction of the dependent variable  $u$  inside each control volume obtained using some set of strategically chosen local cell-average values. The development of high-order schemes has been severely limited by the absence of robust approximation techniques, capable of providing accurate estimates of the successive derivatives of the dependent variable on unstructured grids [9]. Thus the concept of high-order is in general limited in the literature

to formally second-order schemes (piecewise linear reconstruction). Using a Taylor series expansion, the *linear* componentwise reconstruction of the dependent variable inside each cell  $T_i$  is given by

$$u_i(x) = u_i + \nabla u_i \cdot (x - x_{c_i}), \quad (4.8)$$

where  $x_{c_i}$  denotes the centroid of the control volume  $T_i$ , and  $\nabla u_i$  is the gradient of the dependent variable at the centroid. The gradient is assumed to be constant inside each cell and, therefore, the reconstructed variable is still discontinuous across interfaces.

The main difficulty is the accurate evaluation of gradients, and, eventually higher order derivatives. Recently, some authors have proposed gradient approximations using Gauss-Green reconstruction techniques. A second order cell-centered FV scheme based on a linear least square reconstruction is proposed in [3]. A quadratic reconstruction which requires the centroid hessian matrix, has been investigated in [9] using moving least squares approximation techniques. We investigate the possibility to obtain high order gradient and flux approximations, using RBF interpolations and PU strategy.

The system of ordinary differential equations (4.7) can be solved in time using a variety of explicit and implicit time integration schemes. A particularly simple time integration scheme we applied is the well-known forward Euler scheme.

Using the basic finite volume scheme and the forward Euler method, we end up with a first order scheme in space and in time. To improve the time order of convergence we have also applied third order strongly stability preserving Runge Kutta methods.

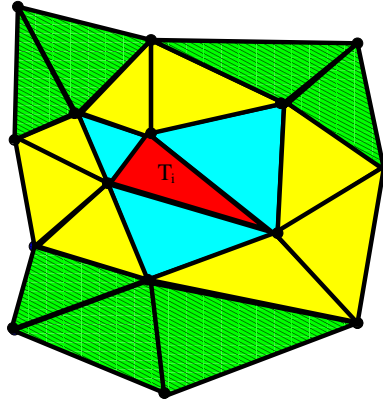
## 5. Optimal recovery using Radial Basis Function

An approximated solution computed by first order schemes is generally considered too inaccurate for most quantitative calculations unless to require very fine meshes thus to make the scheme in general inefficient. For a good reconstruction in regions where the solution of (4.4) is known or expected to be smooth, a higher order reconstruction scheme is desirable. Such high order schemes currently form a major research direction in the theory of finite volume [35].

The accuracy of the basic finite volume method depends crucially on the approximation properties of the cell average operator. To increase the spatial order of accuracy of the basic finite volume method, we reconstruct a piecewise smooth function from the cell averages. This reconstruction is known as *recovery*. Since it is not reasonable to build a reconstruction using all the cell averages, for each cell (triangle  $T_i$ ) a local reconstruction is computed using all the cell averages of cells in a neighborhood of  $T_i$ , that we will denote by *stencil*  $S_i = \{T_1, \dots, T_M\}$ , with  $T_1 = T_i$ . For each stencil,  $h_T$  denotes the length scale associated with each control volume  $T$  in  $S_i$  and  $h = \max_{T \in S_i} h_T$ .

**Definition 5.1.** *On each stencil, a function  $T_i \ni x \mapsto R_i(x)$  is called an  $r$ th-order recovery function if the following conditions hold*

- 1)  $R_i := \frac{1}{|T_i|} \int_{T_i} R(t, x) dx = \bar{u}_i(t) \quad i = 1, \dots, M,$
- 2)  $\lim_{h \rightarrow 0} \|R_i - u\|_{L^\infty(\Omega)} = \mathcal{O}(h^r).$

Figure 1: Stencil associated with triangle  $T_i$ .

The accuracy of the finite volume approximation strongly depends on a combination of high-order flux reconstruction with accurate quadrature rules, as it is stated by the following result, (see [35]).

**Theorem 5.1.** *Assume  $R_i : \mathbb{R}^2 \rightarrow \mathbb{R}$  is an  $r$ th-order recovery function on the triangle  $T_i$  for all  $T_i \in \mathcal{T}$ . Let the weak solution  $u$  as well as the numerical flux  $F(u, u, \mathbf{n})$  be differentiable up to order  $\min\{r, 2ng\}$ . Then  $\forall T_i \in \mathcal{T}$ , the finite volume method*

$$\frac{d\bar{u}_i}{dt} = \frac{1}{|T_i|} \sum_{j \in N(i)} \frac{|e_{ij}|}{2} \sum_{k=1}^{ng} w_k F(R_i(t, p_{i,j}(s_k)), R_j(t, p_{i,j}(s_k)); \mathbf{n}_{ij}), \quad (5.1)$$

has spatial order  $\mathcal{O}(h^{\min\{r, 2ng\})}$ .

In order to avoid unwanted oscillations typical from polynomial interpolation, the ENO approaches select for each cell a set of different stencils, for each stencil a local reconstruction is constructed and then the smoothest (i.e., least oscillatory) is selected, where the smoothness of the polynomial reconstruction is measured by using a suitable oscillation indicator.

We consider the possibility to find local functions with good approximation properties in order to avoid the oscillatory behavior. Supported by numerical experiments, summarized in Section 7, we claim that the use of a suitable large stencil in the radial recovery step, avoids the computational cost of the ENO construction.

For a given triangle  $T_i \in \mathcal{T}$  we construct the stencil  $S_i$  which contains the triangles that share an edge with  $T_i$ , as well as the triangles which share a vertex with  $T_i$ , the triangles which share a vertex with the three upmost adjacent triangles, together with  $T_i$  itself. An example of a stencil is illustrated in Fig. 1. Note that the stencil setting is defined by the PU approach. Instead of using polynomial reconstruction we will use a radial recovery function  $R(x)$  on a triangle  $T_i$  given by

$$R_i(x) = \sum_{j=1}^M \lambda_j L_j^{x_j} \varphi(\|\mathbf{x} - \mathbf{x}_j\|_2), \quad (5.2)$$

where  $\varphi : \mathbb{R}_{\geq 0} \rightarrow \mathbb{R}$  is a radial function and  $M$  is the number of cells in the stencil  $S_i$ . Here  $L^{x_j}$  means the application of the cell average operator to the variable  $\mathbf{x}_j$ . In order to satisfy condition 1) in Definition 5.1, the coefficients  $\lambda_1, \dots, \lambda_M$  in (5.2) are determined by the following recovery conditions on the centers  $\{\mathbf{x}_{c_j}\}_{j=1, \dots, M}$ , that are the centroids of the cells in the stencil

$$L_j R_i = L_j u, \quad j = 1, \dots, M,$$

where  $L_j u$  are the cell averages of the triangles in the stencil. These conditions can be conveniently written in a matrix-vector form

$$A\Lambda = U, \quad A \in \mathbb{R}^{M \times M}, \quad U \in \mathbb{R}^M, \quad \Lambda \in \mathbb{R}^M, \quad (5.3)$$

where  $A = [L_i^x L_j^{x_j} \varphi(\|\mathbf{x} - \mathbf{x}_j\|_2)]_{i,j=1, \dots, M}$ , while the right-hand side is given by  $U = \{\bar{u}_j\}_{j=1}^M$ . In order to compute the elements of  $A$  we need to approximate the term

$$L_j^y \varphi(\|\mathbf{x} - \mathbf{y}\|_2) = \frac{1}{|T_i|} \int_{T_i} \varphi(\|\mathbf{x} - \mathbf{y}\|_2) d\mathbf{y} \quad (5.4)$$

by a midpoint quadrature rule that is

$$L_j^y \varphi(\|\mathbf{x} - \mathbf{y}\|_2) \approx \varphi(\|\mathbf{x} - \mathbf{x}_{c_j}\|_2).$$

The application of the operator  $L_i^x$  is accounted by means of a seven points Gaussian quadrature rule within the triangle  $T_i$ .

Note that, since the vertices of the unstructured given mesh are fixed, the matrices  $A$  for each stencil associated with  $T_i$ , do not change in time and, therefore, they need to be computed only once at the preprocessing phase.

In what follows we will consider special classes of radial functions  $\varphi$  which allow generalized interpolants in the form (5.3), thus we restrict ourselves to positive definite functions, such as inverse multiquadrics:

$$\varphi(r) = 1/\sqrt{r^2 + \gamma^2}, \quad \gamma > 0,$$

Gaussians:

$$\varphi(r) = e^{-\delta r^2}, \quad \delta > 0,$$

and compactly supported radial basis function of continuity  $C^{2\ell}$ :

$$\varphi(r) = (1 - r)_+^{2+2\ell} p(r),$$

where  $p$  polynomial  $\partial p = \ell$ . In these cases,  $A$  is a symmetric positive definite matrix, and the interpolation problem (5.3) is theoretically uniquely solvable [35]. These RBFs do not require to be augmented with the polynomial part which is instead necessary in a general RBF form [18].

Given the radial recovery function (5.2), and considering (5.4), an approximation of  $\nabla R$  is given by

$$\nabla R_i(\mathbf{x}) = \begin{bmatrix} \sum_{j=1}^M \lambda_j \left( \frac{\mathbf{x}^{(1)} - \mathbf{x}_{c_j}^{(1)}}{\|\mathbf{x} - \mathbf{x}_{c_j}\|} \right) \varphi'(\|\mathbf{x} - \mathbf{x}_{c_j}\|) \\ \sum_{j=1}^M \lambda_j \left( \frac{\mathbf{x}^{(2)} - \mathbf{x}_{c_j}^{(2)}}{\|\mathbf{x} - \mathbf{x}_{c_j}\|} \right) \varphi'(\|\mathbf{x} - \mathbf{x}_{c_j}\|) \end{bmatrix}. \quad (5.5)$$

The reconstruction of the gradient of the recovery function  $\nabla R_i$  is used in the flux function  $F$  evaluation. In particular, the points at which  $\nabla R_i$  is actually evaluated are the Gaussian nodes computed by (4.6) on each interior edge of  $T_i$ , thus they lie in the interior of the set of cells in the  $i$ -th stencil. This avoids a well-known problem of RBF interpolations: that of poor accuracy at points near the boundaries.

The radial recovery step takes the cell averages  $\bar{u}_i, i = 1, \dots, \mathcal{N}$ , associated to the triangles  $T_i$  as input and compute the unknowns  $\lambda_j, j = 1, \dots, M$  in (5.3) for each control volume  $T_i$ . The complete semi-discrete finite volume high order scheme is defined as follows.

**Definition 5.2. High Order FV.** *The semi-discrete finite volume approximation of (4.4) utilizing continuous in time solution representation,  $t \in [0, +\infty)$ , and high order radial recovery in space  $u_h$ , such that*

$$\bar{u}_j(t) = \frac{1}{|T_j|} \int_{T_j} u_h(x, t) dx,$$

with initial data  $\bar{u}_j(0) = \frac{1}{|T_j|} \int_{T_j} u_0(x) dx$ , and suitable boundary conditions, is given by the following two steps for each  $T_i \in \mathcal{T}$ :

**STEP 1** *Radial recovery: solve (5.3) for  $\Lambda$*

**STEP 2** *Cell average update: solve the system of ODEs*

$$\frac{d\bar{u}_i}{dt} - \frac{1}{|T_i|} \sum_{j \in N(i)} \frac{|e_{ij}|}{2} \sum_{k=1}^{ng} w_k F(R_i(t, p_{i,j}(s_k)), R_j(t, p_{i,j}(s_k)); \mathbf{n}_{ij}) = \frac{1}{|T_i|} \sum_{j \in N(i)} w_k f_k.$$

A final remark concerns the approximation error between the solution of (4.4) in a Sobolev space  $W_2^k(\Omega)$  of all  $u$  with distributional derivatives  $D^\alpha u \in L_2(\Omega), |\alpha| \leq k$ , and the optimal recovery  $u_h$  given by the High Order FV scheme. At this aim, the weak solution  $u$  is required to be more regular than  $u \in W_2^1(\Omega)$ , more precisely,  $u \in W_2^k(\Omega)$ , with  $k > D/2$ , if  $D$  is the current space dimension. Following [35], under the assumption of  $u \in W_2^k(\Omega)$ , the reconstruction error for  $u_h$  in the finite dimensional subspace  $V_h$  of  $W_2^1(\Omega)$ , can be bounded by

$$\|u - u_h\|_{L_\infty(\Omega)} \leq Ch^{k-1} \|u\|_{W_2^k(\Omega)}. \quad (5.6)$$

This result is applied to the  $C^{2\ell}$  compactly supported RBF with  $\ell \geq k - \frac{D+1}{2}$ , and to the Gaussian RBF, see [35]; for the class of inverse multiquadrics RBF this bound is still an open problem.

## 6. Regularized radial recovery step

Aspects of stability and accuracy of the RBF interpolant involve critical quantities such as the separation distance and the fill distance of a given data set. In particular, the quality of the reconstruction is driven by the fill distance, that is defined as the radius of the largest ball with arbitrary center without any data points in its interior. Dense data set are characterized by a good approximation error. On the other hand, the stability, measured in terms of separation distance, is a serious problem in case of dense data sets. The separation distance is defined as the radius of the smallest ball without any data points in its interior, but with at least two points of the data set on the boundary; therefore, separation distance only depends on the closest pair of points. The condition number of the matrices  $A$  of the linear system (5.3), is extremely large if the separation distance is small. In the case of optimal recovery the conditioning depends on the separation distance of the set of centroids in the stencil. Almost degenerate triangles in a stencil can lead to almost linear dependency of the matrix  $A$  in (5.3).

We refer the reader to [5] for RBF regularization in the interpolation framework.

The linear systems have a special form of degeneration: the large eigenvalues usually are moderate, but there are very small ones leading to bad condition. Therefore it makes sense to go for approximate solutions of the linear systems, for instance by projecting the right-hand sides to spaces spanned by eigenvectors corresponding to large eigenvalues. One way to achieve this is to calculate the singular value decomposition of  $A$  and then use only the subsystem corresponding to large singular values.

A standard regularization strategy to construct a reasonably stable approximation is to choose a positive tolerance and to ignore small singular values, i.e., with absolute value less than the chosen tolerance, because they are usually polluted by roundoff and hardly discernible from zero. This is called the *truncated singular value decomposition (TSVD)* method and it is issued in the present work.

Another popular possibility is the *Tikhonov regularization*, which solves

$$\min_{\Lambda} \|A\Lambda - U\|^2 + \nu \|\Lambda\|^2, \quad (6.1)$$

where  $\nu$  is the positive regularization parameter which value can be determined by different criterium as L-curve or Morozov discrepancy principle, if the noise level is known, or simply experimentally.

The two mentioned regularization methods involve the choice of a parameter, the tolerance in TSVD and the  $\nu$  value in (6.1), which strongly depends on the regularity of the data and thus a wrong choice can affect the solution in a significant way. Therefore, in the following sections, we propose and theoretical justify the least square approximation as a valid alternative to improve the matrix conditioning. Furthermore, we suggest another approach to obtain a regularized solution maintaining an optimal radial recovery step, following the approach proposed in [23].

### 6.1. Regularization by least-squares approximation

Let  $X = X_1 \cup X_2$  be the set of the indices of the centroids in a given stencil consisting of  $M$  triangles. In order to maintain a well-conditioning system, we consider in the set  $X_2$ , only those centroids that provide a separation distance value acceptable among the  $M$  centroids of the entire stencil. Let  $X_1$  be the set of the remaining indexes of the  $\ell \ll M$  centroids discarded from the set  $X$  to increase the separation distance. Without loss of generality, we suppose that  $X_1$  corresponds to the last  $\ell$  columns of  $A$ .

Using this set  $X_1$  we construct the orthonormal columns  $\mathbf{e}_j$ , for each  $j \in X_1$ , of a matrix  $W \in \mathbb{R}^{M \times \ell}$ , as the canonical unit vectors with one in the  $j$ th entry and zeros elsewhere. Hence the span of the orthonormal columns of  $W$  represents the space  $\mathcal{W}$ , corresponding to the elements of  $X_1$ . Let us introduce the orthogonal projectors

$$P_W = WW^T \quad \text{and} \quad P_W^\perp = I - P_W,$$

where  $I$  denotes the identity matrix. We use these projectors to split the solution of the linear system (5.3) according to

$$\Lambda = \Lambda' + \Lambda'', \quad \Lambda' = P_W \Lambda, \quad \Lambda'' = P_W^\perp \Lambda, \quad (6.2)$$

where  $\Lambda'$  represents the critical contribution to the solution that could increase the condition number of the matrix, while  $\Lambda'' \in \mathbb{R}^M \setminus \{\mathcal{W}\}$  is the meaningful part to be considered.

Using the projectors  $P_W$  and  $P_W^\perp$  and the decomposition (6.2), the linear system (5.3) can be rewritten

$$(AP_W + AP_W^\perp)\Lambda = U. \quad (6.3)$$

The regularized solution of (6.3) is now obtained by considering only the second part of the coefficient matrix in (6.3),

$$AP_W^\perp \Lambda = U. \quad (6.4)$$

Taking into account the choice of the projector  $P_W^\perp$  we rewrite (6.4) as the overdetermined linear system

$$B\bar{\Lambda} = U, \quad (6.5)$$

where  $B = AP_W^\perp \in \mathbb{R}^{M \times (M-\ell)}$  contains the  $(M - \ell)$  non-vanishing columns of  $A$ , and  $\bar{\Lambda} \in \mathbb{R}^{(M-\ell)}$ .

Our claim is now that solving the overdetermined linear system (6.5) by least square method, represents a sort of regularization of problem (5.3), that is we improve the conditioning of problem (5.3).

**Theorem 6.1.** *Let  $A \in \mathbb{R}^{M \times M}$  be the coefficient matrix of the linear system (5.3) associated to the set  $X$ , and  $B \in \mathbb{R}^{M \times (M-\ell)}$  the matrix in (6.5), associated to the set  $X_2$ , then  $\text{cond}(B) \leq \text{cond}(A)$ , where  $\text{cond}$  represents the condition number of a matrix.*

*Proof.* The condition number of a rectangular matrix is computed as the quotient of the largest and smallest singular values of the matrix. The result follows from the fact that the

singular values of  $A$  interlace the singular values of sub-matrices of  $A$  consisting of all rows of  $A$  and an increasing number of columns (see [16], p. 449).  $\square$

In general, the least square regularized solution obtained does not strictly satisfy the interpolation conditions given in Definition 5.1 of optimal recovery; nevertheless, as we will demonstrate in Section 7, this will not affect the performance of the PUHOFV proposed method.

## 6.2. Regularization by splitting interpolation

In order to guarantee the optimal recovery, we propose a splitting interpolation scheme applied to improve the conditioning of the linear systems (5.3).

Introduce the QR-factorization

$$AW = QR,$$

where  $Q \in \mathbb{R}^{M \times \ell}$  has orthonormal columns and  $R \in \mathbb{R}^{\ell \times \ell}$  is upper triangular and  $W$  is defined as in the previous section. We will assume that the subspace  $\mathscr{W}$  is chosen so that  $AW$  is of full rank. Then  $R$  is nonsingular. Introduce the orthogonal projectors

$$P_Q = QQ^T \quad \text{and} \quad P_Q^\perp = I - P_Q,$$

and decompose the system (5.3),

$$P_Q A \Lambda' + P_Q A \Lambda'' = P_Q U, \quad (6.6)$$

$$P_Q^\perp A \Lambda'' = P_Q^\perp U, \quad (6.7)$$

where we used that  $P_Q^\perp A P_W = 0$  in the derivation of (6.7). Note that  $\Lambda' \in \mathscr{W}$  represents the part of the solution that can cause instability, while  $\Lambda'' \in \mathbb{R}^M \setminus \mathscr{W}$  is the meaningful well-conditioned part.

Let now  $B = P_Q^\perp A = [b_1 \ \cdots \ b_{M-\ell} \ \cdots \ b_n]$ , represented columnwise, and  $\bar{B} = [b_1 \ \cdots \ b_{M-\ell}] \in \mathbb{R}^{M \times (M-\ell)}$ .

We solve (6.7) for  $\Lambda''$ , in a least square sense by computing

$$B \bar{\Lambda}'' = \bar{U}, \quad (6.8)$$

where  $\bar{U}$  is composed of the first  $M - \ell$  elements of  $P_Q^\perp U$ . Then  $\Lambda'' = [\bar{\Lambda}'' \ \mathbf{0}]$ , which is obtained by adding  $\ell$  zeros to the vector  $\bar{\Lambda}''$ .

**Theorem 6.2.** *Let  $A$  be the coefficient matrix of the linear system (5.3) and  $B$  the matrix in (6.8). Then  $\text{cond}(B) \leq \text{cond}(A)$ .*

*Proof.* Let us first recall that if  $C, D, E \in \mathbb{R}^{M \times M}$  are given matrices, and  $C = DE$  then

$$\rho_{i+j+1} \leq \varrho_{i+1} \sigma_{j+1}, \quad i, j = 0, \dots, M-1, \quad i+j+1 \leq M, \quad (6.9)$$

where  $\rho_i, \varrho_i, \sigma_i$  are the singular values of  $C, D, E$  respectively. Next, let us consider  $C \equiv B, D \equiv P_Q^\perp, E \equiv A$ , and recall that the condition number of a matrix is given by the ratio between the biggest and the smallest singular values. If in (6.9) we consider  $j = 0, i = 0$ , then we get

$$\rho_1 \leq \varrho_1 \sigma_1 = \sigma_1, \quad (6.10)$$

in fact an orthogonal projector has singular values 1 and 0, and  $\rho_1$  and  $\sigma_1$  are the biggest singular values of  $B$  and  $A$ , respectively. Since  $A$  is full rank, we can also write  $D = CE^{-1}$ . From the relation between singular values (6.9)

$$\varrho_{M-\ell} \leq \rho_{M-\ell} \sigma_1^*,$$

where  $\sigma_1^* = 1/\sigma_M$ . Since  $\varrho_{M-\ell} = 1$  we get  $\sigma_M \leq \rho_{M-\ell}$ . Thus, if we consider  $B$  we get (see [4]):

$$\text{cond}(B) = \frac{\rho_1}{\rho_{M-\ell}} \leq \frac{\sigma_1}{\sigma_M} = \text{cond}(A).$$

This completes the proof of the theorem.  $\square$

Then  $\Lambda'$  is obtained by (6.6). In fact, Eq. (6.6) has a coefficient matrix of small dimension  $\ell \times \ell$  and can be expressed as

$$Rz' = Q^T(U - A\Lambda''). \quad (6.11)$$

We compute the solution  $z'$  of (6.11), and then we evaluate

$$\Lambda' = Wz'. \quad (6.12)$$

The final computed solution  $\Lambda$  of linear system (5.3), that gives RBF coefficients with interpolation conditions, can now be obtained by summing up the two approximations  $\Lambda'$  and  $\Lambda''$ . Experimental results demonstrate that we improve the condition number of the linear system of at least two orders of magnitude.

## 7. Applications and numerical results

In this section, we evaluate and validate the strategies described in the previous sections by using two numerical experiments. In the first experiment, the accuracy and convergence is analyzed by considering a diffusion problem which allows us to compare the numerical results with the analytical solution. In the second experiment, we apply the discussed PUHOFV strategies to a couple of PDE second order models for the specific problem of noise removal on images and functional surfaces defined, respectively, on structured and unstructured meshes. This illustrates the efficacy of the high order optimal recovery strategies in real cases, compared with the basic FV schemes.

### 7.1. Experimental Order of Convergence (EOC)

In this experimental section we consider the isotropic diffusion equation of the form

$$\frac{\partial u}{\partial t} = \nabla \cdot (\nabla u), \quad (7.1)$$

for a compact time interval  $I = [0, t_{MAX}]$ , and the computational domain  $\Omega = [0, 1] \times [0, 1]$ . In case of initial conditions

$$u(0, x) = \cos(2\pi x) \cos(\pi y), \quad (7.2)$$

and homogeneous Neumann boundary conditions, the exact scalar solution  $u : I \times \Omega \rightarrow \mathbb{R}$  of (7.1) is given by

$$u(t, x) = \cos(2\pi x) \cos(\pi y) e^{-5\pi^2 t}. \quad (7.3)$$

We consider the solution of Eq. (7.1) by a FV discretization scheme applied to a nested sequence of four regular grids with mesh width  $h$ . In particular, mesh sizes  $h = 0.1, 0.05, 0.025, 0.0125$  form square grids of size  $n \times n$ , respectively,  $10 \times 10, 20 \times 20, 40 \times 40, 80 \times 80$ . We let  $t_{MAX} = 5 \cdot 10^{-3}$  and we compute the time step  $\tau$  in such a way to guarantee the CFL condition  $\tau \leq h^2/4$  for the explicit forward Euler time discretization.

In order to measure the accuracy of the approximate solution  $u_h$  on a mesh of width  $h$  we measure the errors

$$E_2(h) = \frac{\|u - u_h\|_2}{\mathcal{N}}, \quad E_g(h) = \frac{\|\nabla u - \nabla u_h\|_2}{\mathcal{N}_e}, \quad (7.4)$$

where  $u$  is the exact solution,  $\mathcal{N}$  is the number of triangles of the mesh, and  $\mathcal{N}_e$  is the number of internal edges in the mesh.

The reconstruction of edge-centered gradients  $\nabla u_h$  is obtained by the radial recovery function and its approximation of  $\nabla R$  given by (5.5).

In order to estimate the convergence, the *experimental order of convergence* (EOC), identified as the parameter  $\alpha$  in the formula

$$Error(h/2) = C(h/2)^\alpha, \quad (7.5)$$

can be determined by comparing numerical solutions and exact solution on subsequently refined grids

$$\alpha = \log_2(E_2(h)/E_2(h/2)). \quad (7.6)$$

The same formula for  $E_g$  instead of  $E_2$ , makes it possible to estimate the convergence rate of the edge-centered gradient approximations.

Tables 1, 2, and 3 show the dependence of the errors (7.4) in  $L_\infty((0, t_{MAX}), L_2(\Omega))$ -norm on the mesh size, for subsequently refined/denser grids, together with the corresponding convergence orders  $\alpha$ .

In Table 1 the optimal recovery step is based on an RBF interpolation, while in Table 2 the results report the convergence in case of least squares approximation in the radial

Table 1: Convergence results for regular meshes using a PUHOFV discretization and interpolation recovery step.

Grid size	$\tau$	$E_2(h)$	$\alpha$	$E_g$	$\alpha$
10 × 10	$2.50 \times 10^{-4}$	$2.90 \times 10^{-3}$	–	0.0775	–
20 × 20	$6.25 \times 10^{-5}$	$3.38 \times 10^{-4}$	3.10	0.0236	1.71
40 × 40	$1.56 \times 10^{-5}$	$3.82 \times 10^{-5}$	3.14	0.0094	1.33
80 × 80	$3.90 \times 10^{-6}$	$7.98 \times 10^{-6}$	2.26	0.0035	1.42

Table 2: Convergence results for regular meshes using a PUHOFV discretization and least squares radial recovery step.

Grid size	$\tau$	$E_2(h)$	$\alpha$	$E_g$	$\alpha$
10 × 10	$2.50 \times 10^{-4}$	$2.70 \times 10^{-3}$	–	0.0768	–
20 × 20	$6.25 \times 10^{-5}$	$4.44 \times 10^{-4}$	2.60	0.0245	1.64
40 × 40	$1.56 \times 10^{-5}$	$4.96 \times 10^{-5}$	3.16	0.0096	1.35
80 × 80	$3.90 \times 10^{-6}$	$4.38 \times 10^{-6}$	3.50	0.0035	1.45

Table 3: Convergence results for irregular meshes using a PUHOFV discretization and interpolation recovery step.

$\mathcal{N}_v/\mathcal{N}$	$\tau$	$E_2(h)$	$\alpha$	$E_g$	$\alpha$
100/183	$7.48 \times 10^{-7}$	$2.7 \times 10^{-3}$	–	0.0820	–
400/776	$8.77 \times 10^{-8}$	$3.69 \times 10^{-4}$	2.50	0.0367	1.16
1600/3169	$3.31 \times 10^{-9}$	$8.84 \times 10^{-5}$	2.43	0.0126	1.54

recovery step (see Section 6.1). The results show that our scheme reaches an expected order of convergence greater than 2 even in case of approximated optimal recovery. It should be observed that the  $\|\nabla u_h\|_{\mathcal{T}_h}$  always remains limited in the evolution, as a confirm of a limited total variation of  $u_h$ .

To the aim to investigate the influence of mesh irregularity on the accuracy of the proposed PUHOFV discretization scheme, we apply the scheme for solving (7.1) on a sequence of four irregular meshes with a number of control volumes (triangles) close to the regular case (Table 1). The time step  $\tau$ , in the forward Euler time discretization, is chosen so that  $\tau \leq \frac{1}{4} \min(h)$ , where  $h$  is the height of the mesh triangles. In Table 3 we report the dependence of the errors (7.4) in  $L_\infty((0, t_{MAX}), L_2(\Omega))$ -norm on the mesh size, for meshes of increasing density measured by  $\mathcal{N}_v$  vertices and  $\mathcal{N}$  triangles, together with the corresponding convergence orders  $\alpha$ .

The results in Table 3 confirm the ability of the method to achieve high accuracy on relatively coarse meshes even in case of irregular meshes. The convergence orders are slightly lower in the irregular case due to the higher number of time steps required in case of the irregular meshes in order to reach the stopping criterion  $t_{MAX}$ . This leads to a propagation of time inaccuracy amplified by an eventually bad conditioned radial recovery step based on RBF interpolation. This will be discussed in detail in Section 7.2. In this case, the convergence can easily be improved by using a more accurate discretization in time, such as, for example, a third order stability preserving Runge Kutta method.

The approximated solution obtained by PUHOFV space discretization of the PDE model

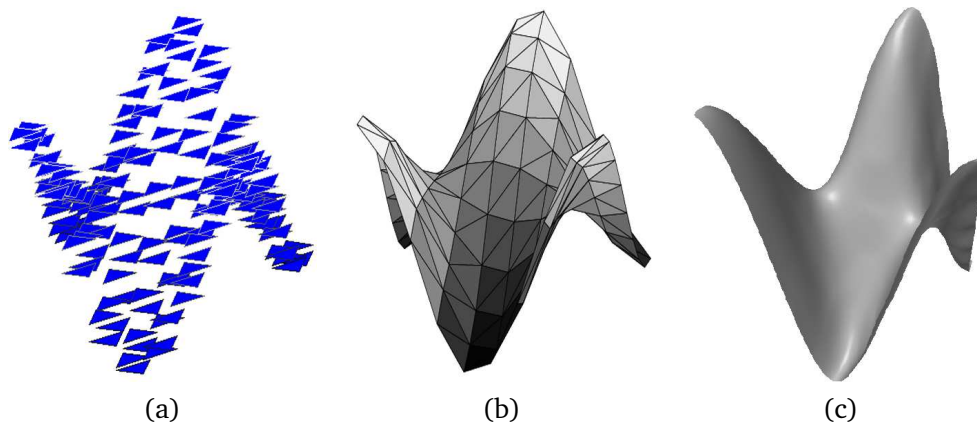


Figure 2: Reconstructed solution: (a) cell-averaged solution; (b) linearly reconstructed vertex values; (c) PU reconstructed vertex cell-averaged values.

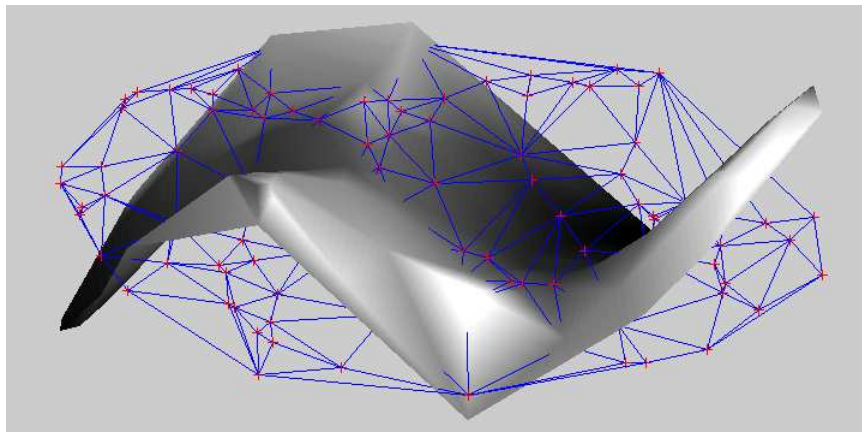


Figure 3: Initial condition  $u_0$  for the PDE model (7.1) on the irregular mesh.

(7.1) on a regular mesh  $20 \times 20$ , is displayed in Fig. 2. This figure depicts, from left to right, the piecewise constant cell-averaged solution, Fig. 2(a), the linearly-reconstructed values at the mesh vertices obtained by (4.8), Fig. 2(b), while Fig. 2(c) shows the solution provided by the PU reconstruction using the cell averaged values  $u_i^k$  in (3.1) obtained by radial optimal recovery.

## 7.2. Effect of the regularization

The conditioning of the linear systems (5.3) in radial recovery will get extremely large if the separation distance of the set of centroids of the domain mesh gets small. Nevertheless, no matter what the condition number of the linear system is, we always get good approximate solutions if the RBF is suitably scaled in the domain. This unexpected robust behavior is obtained with noisy-free right-hand side, but it is extremely sensitive to the

noise. In case of radial recovery step in evolutionary PDE, the noise can be represented either by noise on the initial data set, or by the perturbation propagated in time by a non-accurate time discretization method, such as, for example, the forward Euler method. The former aspect will be investigated in Section 7.3, while the latter will be addressed in the remaining of this section. In all these noisy situations, interpolation should be replaced by approximation. Interpolation of noisy data in fact could lead the simulation to run into severe numerical instability.

Let us consider the noisy-free problem (7.1) with analytic solution (7.3). Unlike the test case in Section 7.1, where we considered a structured grid of increasing dimension, in this case we evaluate the analytical function  $u_0$  at the vertices of an irregular mesh randomly constructed with 100 vertices and 189 triangles. Fig. 3 shows  $u_0$  together with the associated irregular mesh.

The test problem (7.1) is solved by a PUHOFV discretization in space and a forward Euler in time, considering a time step  $\tau$  chosen so that  $\tau \leq \frac{1}{4} \min(h)$ , where  $h$  is the height of the mesh triangles. The structure of the stencil is described in Section 5, thus the number of triangles in each stencil is between a minimum of 10 and a maximum of 20, and this corresponds to the number of unknowns in the linear systems (5.3).

We want to compare the different regularization approaches discussed in Section 6 in case of bad conditioning. To this aim, we built the mesh in Fig. 3 with several very close vertices which cause a small separation distance and thus a bad conditioning. In particular, the condition numbers of the linear systems (5.3) are in the range  $[6.97 \times 10^7, 9.54 \times 10^{13}]$ , where 153 on the total 189 linear systems have a condition number greater than  $10^{10}$ .

Using the interpolation recovery step, the ill conditioning is propagated in the evolution and it amplifies the propagated errors due to inaccuracy of the forward Euler time discretization. After 100 time steps this causes the fail of the convergency and the error starts to increase.

Then we replace the interpolation recovery step with a TSVD regularization as described in Section 6, using a tolerance  $1 \times 10^{-4}$ , after 1200 steps we get  $E_2 = 0.0052$ ,  $E_\infty = 0.6989$ , and  $E_g = 0.0867$ . The evolution converges to the exact solution at the given  $t_{MAX}$ .

Finally, the interpolation recovery step is replaced by least squares approximation where the centers are selected between the centroids of the stencil so that to increase the separation distance inside the stencil (see Section 6.1). After 1200 steps we get  $E_2 = 0.0027$ ,  $E_\infty = 0.1754$ , and  $E_g = 0.0628$ . The evolution converges to the exact solution at the given  $t_{MAX}$ .

We can then conclude that in case of well conditioning, that is an irregular distribution of nodes of the mesh that does not cause a particularly small separation distance, the interpolation optimal recovery gives the best accurate reconstruction with respect to any regularized and thus approximated reconstruction. In case of unstructured mesh that could lead to bad conditioning, both TSVD and least squares approximation can be used to avoid instabilities. The latter is parameter free, and this can be considered a good advantage, moreover it provides slightly better results.

### 7.3. Denoise of surfaces and images

Removal of noise is a necessary pre-processing step for several surface processing tasks such as surface reconstructions, curvature detections, structure recognition, and so on. In this section we consider the problem of denoising images and functional surfaces that are typical from range image 3D scanners acquisition systems, where the range image represents an unstructured set of scalar values corresponding to a set of points on a 3D acquisition plane. In general the points are corrupted by measurement errors.

A common way to represent bivariate data such as height fields and grey-scale images is the so-called *functional surface*  $S(x, y, u(x, y))$  defined along the  $xy$ -plane, by an intensity function  $u : \Omega \subset \mathbb{R}^2 \rightarrow \mathbb{R}$ . An image can be interpreted as a discretization of a continuous function defined on  $\Omega \subset \mathbb{R}^2$  by assigning the image intensity to the elevation along the  $z$  direction. By introducing the function  $d(x, y, z) = z - u(x, y)$  then the surface  $S$  is implicitly defined by  $d(x, y, z) = 0$ .

We are interested in restoring a functional surface  $d(x, y, z)$  which is corrupted by noise in such a way that the process should recover the main structures of the surface.

We apply the model proposed in [24], which generalizes [20, 21], and is based on the reconstruction of a noise-reduced surface from the smoothed normal field, considering a curvature preserving term.

The first step involves the smoothing of the normal vectors  $\mathbf{n}_0 = \nabla d_0 / |\nabla d_0|$  minimizing the functional:

$$\inf_{|\mathbf{n}|=1} \left\{ \int_{\Omega} |\nabla \mathbf{n}| dx + \frac{a}{2} \int_{\Omega} |\mathbf{n} - \mathbf{n}_0|^2 dx \right\}, \quad (7.7)$$

where  $a > 0$  is a parameter that balances smoothing and fidelity to the original vector field. The second step recovers the functional surface from the smoothed normal field that results from solving (7.7), by minimizing the functional

$$\inf_d \left\{ \int_{\Omega} (|\nabla d| - \nabla d \cdot \mathbf{n}) dx + \int_{\Omega} g(\text{curv}_S) |\nabla d| dx + \frac{b}{2} \int_{\Omega} (|d - d_0|^2 - \sigma^2) dx \right\}, \quad (7.8)$$

where  $b > 0$ , is a given parameter,  $\sigma$  is a fairly accurate bound of the norm of the noise, and

$$\begin{aligned} \text{curv}_S &= \text{div}(\mathbf{n}) = \text{div} \left( \frac{(-u_x, -u_y, 1)}{\sqrt{1 + u_x^2 + u_y^2}} \right) \\ &= \frac{(1 + u_y^2)u_{xx} - 2u_x u_y u_{xy} + (1 + u_x^2)u_{yy}}{(1 + u_x^2 + u_y^2)} \end{aligned} \quad (7.9)$$

is the mean curvature of the functional surface  $S$ . The central functional term in (7.8) has been introduced to obtain curvature driven diffusion. The diffusivity function  $g(\cdot)$  considered in this work is the well-known Perona Malik diffusivity,

$$g(s) = \frac{1}{(1 + s^2/K^2)}, \quad K > 0.$$

This results into two coupled non-linear second order PDEs [24]. In the remaining of this section we will refer to this PDE model as the *two-step model*.

In the following examples, noisy functional surfaces have been obtained by adding an error vector  $\eta$  with normally distributed random entries with zero mean to the functional values  $z$ . In Eq. (7.8) we set  $b = 1$ . The vector  $\eta$  is scaled to correspond to a specified noise level  $\mu = \|\eta^\sigma\|/\|z\|$ . According to the notation in Section 4, for the compactly supported RBFs we set  $\ell = 4$ , for the Gaussian RBFs we set  $\delta = 0.5$ , while for the inverse multiquadrics we set  $\gamma = 0.5$ . All computations are carried out in MATLAB, version R2007a, with machine epsilon  $\epsilon \approx 2 \cdot 10^{-16}$ .

**Example 7.1.** The above described two-step model can be simply applied to the classical image denoising problem where the underlying domain turns out to be a rectangular structured grid. In this example we consider the denoise of a gray-scale image which is interpreted as a functional surface by assigning the image intensity to the elevation along the  $z$  direction of the  $xy$  image plane.

A test image has been used as a functional surface to show the effectiveness of the curvature term introduced in the two-step model (7.8). The noise-free image of size  $100 \times 100$  pixels is shown in Fig. 4 (first row, left). The noisy-free associated functional surface, shown in Fig. 4 (first row, center), is defined on a structured grid of 10000 vertices and 19602 triangles. The perturbed surface obtained by considering a noise level  $\mu = 1 \cdot 10^{-2}$  is shown in Fig. 4 (first row, right). The first step in the two-step model (7.7) is initialized with a normal perturbed vector field  $\mathbf{n}_0$  illustrated in Fig. 4 (second row, left), while the resulting smoothed normal vector fields obtained after 4 and 8 time steps, with  $\tau = 1 \cdot 10^{-4}$  are shown in Fig. 4 (second row, center and right, respectively). The reconstructed surface obtained applying the second step (7.8) without curvature contribution after 8 time steps is shown in Fig. 4 (third row, left), while the reconstructions shown in Fig. 4 (third row, center and right) have been obtained by including  $g(\text{curv}_S)$  after 4 and 10 time steps, respectively. A PUHOFV scheme has been used for the space discretization using inverse multiquadrics RBF.

**Example 7.2.** To demonstrate the effectiveness of the High Order FV scheme we compare the results obtained by the sophisticated two-step model (7.7) and (7.8), with the results obtained using the standard Total Variation (TV) model

$$\frac{\partial u}{\partial t} - \nabla \cdot \left( \frac{\nabla u}{|\nabla u|} \right) = 0, \quad (7.10)$$

see [34] for reference. The TV model is applied to the damaged surface *fish*, shown in Fig. 5(a), defined on an unstructured grid of 13208 triangles and 6833 vertices, corrupted by a noise level  $\mu = 1 \cdot 10^{-2}$ , with the aim to recover a noisy-free surface. In Fig. 5(b) the reconstruction using the two-step model after 10 time steps is illustrated, while in Fig. 5(c) the surface obtained after 10 time steps of the TV model is shown. The satisfactory reconstruction we get after only a few steps can be motivated by the use of PUHOFV scheme, using Gaussian RBF recovery strategy.

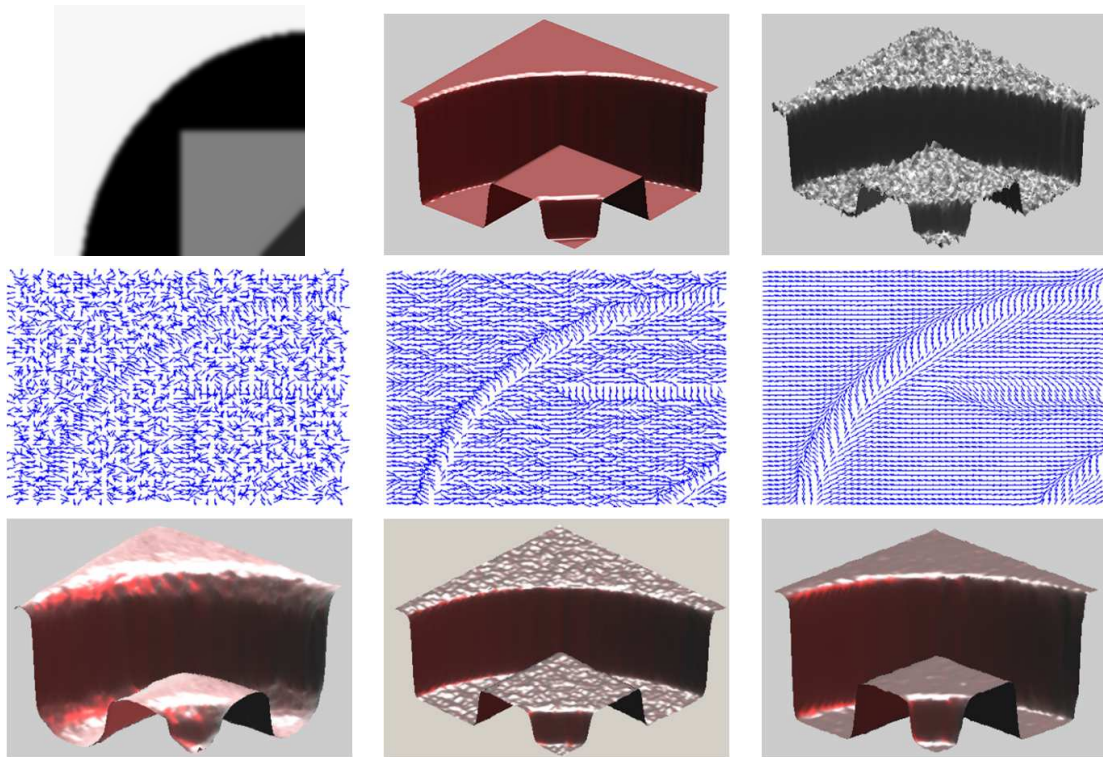


Figure 4: Example 7.1: (first row) noise-free image; associated uncorrupted functional surface; damaged functional surface; (second row) initial perturbed normal field; smoothed normal field by (7.7), time step 4; smoothed normal field by (7.7), final time step; (third row) reconstructed surface using model (7.8) without curvature contribution; reconstructed surface with curvature term  $g(curv_s)$ , intermediate and final time steps.

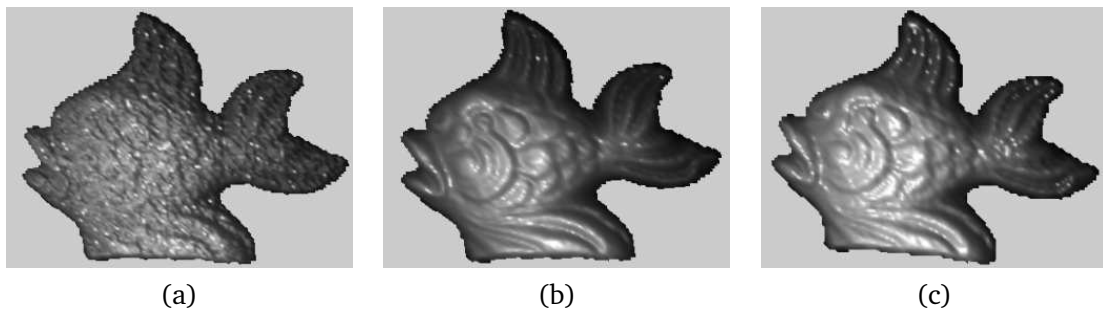


Figure 5: Example 7.2: (a) corrupted surface fish with noise level  $1 \cdot 10^{-2}$ ; (b) reconstructed surface applying the two-step model; (c) reconstructed surface obtained by the TV model.

**Example 7.3.** In the third test we consider a noise-free surface, obtained by the data set `angel`, defined on a grid of 5000 triangles and 2601 vertices. Additive white noise with noise level  $\mu = 5 \cdot 10^{-3}$  is added in the  $z$  direction. The noisy surface is shown in Fig. 6(a). The curvature map represented as a gray-level image is depicted in Fig. 7; it

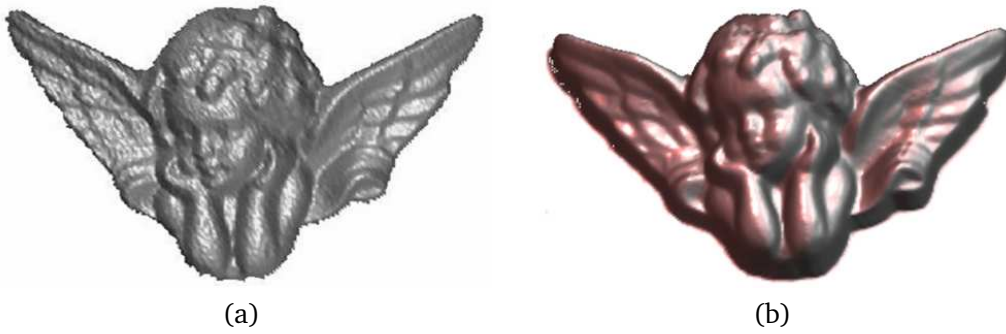


Figure 6: Example 7.3: (a) corrupted surface `angel` with noise level  $5 \cdot 10^{-3}$ ; (b) reconstructed surface using PUHOFV scheme on the two-step model, after 10 time steps.



Figure 7: Example 7.3: curvature map.

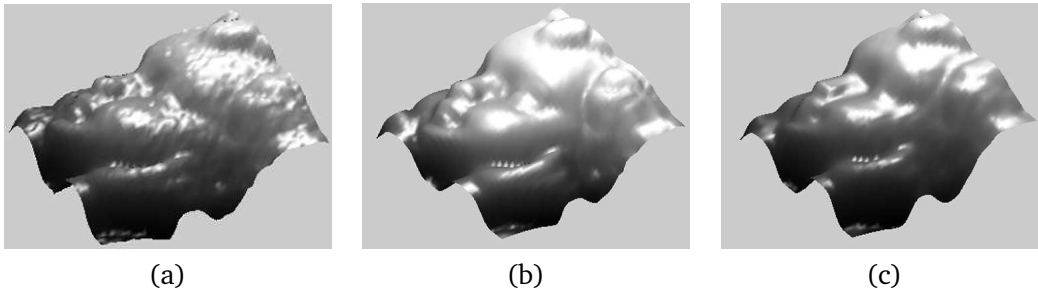


Figure 8: Example 7.3: (a) a detail from the corrupted surface `angel`; (b) reconstructed surface detail using PUHOFV scheme for the two-step model; (c) reconstructed surface detail using PUHOFV discretization for the TV model.

is reconstructed through the smoothed normal field and used in the second step of the two-step model. Applying the two step model discretized by PUHOFV scheme, after 10 time steps we get the smoothed version of the damaged `angel` surface shown in Fig. 6(b). The image in Fig. 8(a) shows a detail from the corrupted noisy `angel` surface. The surface detail reconstructed applying the two-step model discretized with PUHOFV scheme is shown in Fig. 8(b); we used Inverse Multiquadrics RBF in the optimal recovery steps. The same reconstructed detail using the TV model, discretized by PUHOFV scheme is shown in Fig. 8(c). Visual inspection shows a very good reconstruction after only a few time steps.

## 8. Conclusions and ongoing Work

In this paper we investigated a high order cell-centered finite volume scheme for diffusion PDE models obtained by combining the use of RBF optimal recovery with Gaussian quadrature integration methods. The cell averaged results can be assembled together in a powerful partition of unity framework which provides high quality reconstructions. The resulting finite volume discretization leads to an accurate numerical solution without the need for excessively small mesh spacing with a modest additional overhead. In case of severe irregular unstructured meshes, a least square-based approach is provided to obtain a robust regularized solution. An ongoing work will proceed with the study of a posteriori error control strategies for finite volume approximations and the use of it for adaptive numerical techniques.

**Acknowledgments** This work has been supported by PRIN-MIUR-Cofin 2006, project and by University of Bologna "Funds for selected research topics".

## References

- [1] I. Babuska and J.M. Melenk, The Partition of Unity method, *Int. J. Numer. Meths Eng.*, **40**, pp.727–758 (1997).
- [2] T.J. Barth and P.O. Frederickson, Higher Order Solution of the Euler Equations on Unstructured Grids Using Quadratic Reconstruction, AIAA paper 90-0013, Jan. 1990.
- [3] E. Bertolazzi and G. Manzini, Least square-based finite volumes for solving the advection-diffusion of contaminants in porous media, *Applied Numerical Mathematics*, **51**, pp.451–461 (2004).
- [4] D. Bini, M. Capovani and O. Menchi, Metodi Numerici per L'algebra Lineare, *Zanichelli (eds.)*, (1993).
- [5] G. Casciola, L.B. Montefusco and S. Morigi, The regularizing properties of anisotropic Radial Basis Functions, *Applied Mathematics and Computation*, **190/2**, pp.1050–1062 (2006).
- [6] G. Casciola, D. Lazzaro, L.B. Montefusco and S. Morigi, Shape preserving surface reconstruction using locally anisotropic RBF Interpolants, *Computer and Mathematics with Applications*, **51**, pp.1185–1198 (2006).
- [7] U. Clarenz, U. Diewald and M. Rumpf, Nonlinear anisotropic diffusion in surface processing, In *(T. Ertl, B. Hamann and A. Varshney, eds.) Proceedings of IEEE Visualization 2000*, pp. 397–405 (2000).
- [8] S. Corsaro, K. Mikula, A. Sarti and F. Sgallari, Semi-implicit co-volume method in 3D image segmentation, *SIAM Journal on Scientific Computing*, **28/6**, pp. 2248–2265 (2006).
- [9] L. Cueto-Felgueroso, I. Colominas, J. Fe, F. Navarrina and M. Casteleiro, High-order finite volume schemes on unstructured grids using moving least-squares reconstruction. Application to shallow water dynamics, *Int. Journal for Numerical Methods in Engineering*, **65**, pp. 295–331 (2006).
- [10] M. Dumbser and M. Kaser, Arbitrary high order non-oscillatory finite volume schemes on unstructured meshes for linear hyperbolic systems, *Journal of Computational Physics*, **221**, pp. 693–723 (2007).
- [11] G.E. Fasshauer, Solving differential equations with radial basis functions: Multilevel methods and smoothing, *Adv. Comput. Math.*, **11**, pp. 139–159 (1999).

- [12] C. Franke and R. Schaback, Solving partial differential equations by collocation using radial basis functions, *Appl. Math. Comput.*, **93**, pp. 73–82 (1998).
- [13] M. Floater and A. Iske, Multistep scattered data interpolation using compactly supported radial basis functions, *J. Comput. Applied Math.*, **73**, pp. 65–78 (1996).
- [14] M. Griebel and M.A. Schweitzer, A particle-partition of unity method for the solution of elliptic, parabolic and hyperbolic PDE, *SIAM J. Sci. Comp.*, **22/3**, pp. 853–890 (2000).
- [15] M. Griebel and M.A. Schweitzer, A particle-partition of unity method - part II: efficient cover construction and reliable integration, *SIAM J. Sci. Comp.*, **23/5**, pp. 1655–1682 (2002).
- [16] G.H. Golub and C.F. Van Loan, *Matrix Computations*, 3rd ed., Johns Hopkins University Press, Baltimore, 1996.
- [17] A. Handlovcova, K. Mikula and F. Sgallari, Semi-implicit complementary volume scheme for solving level set like equations in image processing and curve evolution, *Numerische Mathematik*, **93/4**, pp. 675–695 (2003).
- [18] A. Iske and T. Sonar, On the structure of function spaces in optimal recovery of point functionals for ENO-schemes by radial basis functions, *Num. Math.*, **74**, pp. 177–201 (1996).
- [19] M. Junk, Do finite volume methods needs a mesh?, In: *Meshfree Methods for Partial Differential Equations*, M. Griebel, M.A. Schweitzer (eds.), Springer, pp. 223–238 (2003).
- [20] D. Krishnan, P. Lin and X.C. Tai, An efficient operator splitting method for noise removal in images, *Commun. Comput. Phys.*, **1**, pp. 847–858 (2006).
- [21] M. Lysaker, S. Osher and X.C. Tai, Noise removal using smoothed normals and surface fitting, *IEEE Transactions on Image Processing*, **13/10**, pp. 1345–1357 (2004).
- [22] K. Mikula, A. Sarti and F. Sgallari, Co-volume method for Riemannian mean curvature flow in subjective surfaces multiscale segmentation, *Computing and Visualization in Science*, **9/1**, pp. 23–31 (2006).
- [23] S. Morigi, L. Reichel and F. Sgallari, Orthogonal projection regularization operators, *Numer. Algorithms*, **44**, pp. 99–114 (2007).
- [24] S. Morigi and F. Sgallari, A high order finite co-volume scheme for denoising using Radial Basis Functions, *Lecture Notes in Computer Science Vol. 4485, Scale Space and Variational Methods in Computer Vision*, F. Sgallari, A. Murli and N. Paragios Eds., pp. 43–54 (2007).
- [25] T.J. Moroney and I.W. Turner, A three-dimensional finite volume method based on radial basis functions for the accurate computational modelling of nonlinear diffusion equations, *Journal of Computational Physics*, **225**, pp. 1409–1426 (2007).
- [26] K.W. Morton and T. Sonar, Finite volume methods for hyperbolic conservation law, *Acta Numerica*, pp. 155–238 (2007).
- [27] Y. Ohtake, A. Belyaev, M. Alexa, G. Turk and H.P. Seidel, Multi-level partition of unity implicits, *ACM Transaction on Computer Graphics*, **22/3**, pp. 463–470 (2003).
- [28] P. Perona and J. Malik, Scale-space and edge detection using anisotropic diffusion, *PAMI*, **12/7**, pp. 629–639 (1990).
- [29] R.J. Renka, Multivariate interpolation of large sets of scattered data, *ACM Transaction on Mathematical Software*, **14/2**, pp. 139–148 (1988).
- [30] R. Schaback, Error estimates and condition numbers for radial basis function interpolation, *Adv. Comput. Math.*, **3**, pp. 251–264 (1995).
- [31] R. Schaback, Stability of radial basis function interpolants, In *Approximation Theory X: Wavelets, Splines, and Applications*, (Edited by C.K. Chui et al.), pp.433–440, Vanderbilt Univ. Press, Nashville (2002).
- [32] T. Sonar, Optimal recovery using thin plate splines in finite volume methods for the numerical solution of hyperbolic conservation laws, *IMA Journal of Numer. Analysis*, **16**, pp. 549–581 (1996).

- [33] T. Sonar, Chapter 3, Methods on unstructured grids, WENO and ENO recovery techniques, in *Hyperbolic Partial Differential Equations: Theory, Numerics and Applications*, (A. Meister and J. Struckmeier, eds.), Vieweg, pp. 115–232 (2002).
- [34] L. Rudin, S. Osher and E. Fatemi, Nonlinear total variation based noise removal algorithms, *Physica D*, **60**, pp. 259–268 (1992).
- [35] H. Wendland, On the convergence of a general class of finite volume methods, *SIAM J. Numerical Analysis*, **43**, pp. 987–1002 (2005).